Visible Wavelength Planar Metalenses Based on Titanium Dioxide

Mohammadreza Khorasaninejad, Wei Ting Chen, Alexander Y. Zhu, Jaewon Oh, Robert C. Devlin, Charles Roques-Carmes, Ishan Mishra, and Federico Capasso, *Fellow, IEEE*

(Invited Paper)

***Abstract*—We present recent advances in metasurface-based photonics, which enables the realization of high performance planar lenses (metalenses) in the visible spectrum. They are enabled by a technique based on atomic layer deposition of titanium dioxide allowing for the fabrication of nanostructures with high fidelity. First, we demonstrate highly efficient metalenses with numerical aperture $\mathrm{NA} = 0.8$ using the Pancharatnam-Berry phase approach. These metalenses can focus light into a diffraction-limited spot. They have efficiencies as high as 86% and provide high imaging resolution. Furthermore, by judicious design of the phase-shifting elements, we achieve a multispectral chiral metalens realized with a single metasurface layer. This chiral metalens can resolve both the chiral and spectral information of an object without the requirement of any additional optical components. Finally, we discuss the experimental realization of polarization-insensitive metalenses with NAs as high as 0.85. They are able to focus incident light to a spot as small as $\sim 0.64\lambda$ with efficiencies up to 60%. Due to its straightforward and CMOS-compatible fabrication, this platform is promising for a wide range of applications ranging from camera modules, displays, laser-based imaging, microscopy, and spectroscopy to laser fabrication and lithography.**

***Index Terms*—Chirality, diffractive optics, diffraction-limited focusing, high resolution imaging, metasurface, planar lenses, polarization resolved imaging, visible spectrum.**

I. Introduction

CONTROL over the amplitude, direction, and polarization of light is the basic principle behind optical design. Traditionally this has been achieved via shaping bulk materials into specific geometries (e.g. lenses, prisms based on refractive optics) and utilizing their intrinsic material properties (e.g. polarizers, waveplates). However, this approach requires relatively long propagation lengths (on the order of many wavelengths) to mold the wavefront, resulting in bulky components. This prohibits the miniaturization of optical systems where several such components generally need to be cascaded to achieve a desired functionality. As a result, there has been a continuous effort to reduce the optical path and ultimately achieve ultra-thin components. Diffractive optics has been a pioneering approach toward this goal with the development of gratings [1]–[8] and lenses [6], [7], [9]–[11]. The advent of metamaterials [12]–[27] has added another dimension to wavefront control by introducing the meta-atom concept. In contrast to natural materials, the optical properties of metamaterials are determined by the geometrical structure of the meta-atom rather than the materials used. This breaks away from the constraints imposed by naturally available materials. The judicious assembly of these meta-atoms not only controls the wavefront of light but also achieves optical properties not possible with conventional approaches (e.g. diffractive optics). These include cloaking [28]–[32], negative refraction [13]–[16], [19] and super/hyper lensing [33]–[38]. Subsequently, their two-dimensional counterparts—metasurfaces [38]–[45], have attracted significant attention mainly due to their relative ease of fabrication and further reduction in spatial footprint. The building block of metasurfaces are subwavelength-structures (SWS) patterned on an interface. By appropriately adjusting their size, orientation, geometry and arrangement, one can control/change the fundamental properties of incident light and thus modify the wavefront to desired specifications. Due to the numerous degrees of freedom in design for SWS, it is also possible to achieve multifunctional devices with a single metasurface, for example using transformation optics [46]. Many different optical components such as planar

Manuscript received August 15, 2016; revised September 30, 2016; accepted October 3, 2016. Date of publication October 11, 2016; date of current version December 29, 2016. This work was supported in part by the Air Force Office of Scientific Research (MURI, Grants FA9550-14-1-0389 and FA9550-16-1-0156), in part by Charles Stark Draper Laboratory, Inc. (SC001-0000000959), and in part by Thorlabs, Inc. The work of W. T. Chen was supported by the postdoctoral fellowship from the Ministry of Science and Technology, Taiwan (104-2917-I-564-058). The work of A. Y. Zhu was supported by Harvard SEAS and A*STAR Singapore under the National Science Scholarship scheme. The work of R. C. Devlin was supported by Charles Stark Draper Fellowship. This work was performed in part at the Center for Nanoscale Systems (which is a part of Harvard University), a member of the National Nanotechnology Coordinated Infrastructure, which was supported by the National Science Foundation under NSF Award. 1541959.

M. Khorasaninejad, W. T. Chen, A. Y. Zhu, R. C. Devlin, and F. Capasso are with Harvard John A. Paulson School of Engineering and Applied Sciences, Harvard University, Cambridge, MA 02138 USA (e-mail: khorasani@seas.harvard.edu; weitingchen@seas.harvard.edu; azhu01@g.harvard.edu; devlin@fas.harvard.edu; capasso@seas.harvard.edu).

J. Oh was with Harvard John A. Paulson School of Engineering and Applied Sciences, Harvard University, Cambridge, MA 02138 USA. He is now with the University of Waterloo, Waterloo, ON N2L 3G1, Canada (e-mail: j3oh@uwaterloo.ca).

C. Roques-Carmes is with Harvard John A. Paulson School of Engineering and Applied Sciences, Harvard University, Cambridge, MA 02138 USA, and also with the École Polytechnique, Palaiseau 91120, France (e-mail: charles.roques-carmes@polytechnique.edu).

I. Mishra is with Harvard John A. Paulson School of Engineering and Applied Sciences, Harvard University, Cambridge, MA 02138 USA, and also with the University of Waterloo, Waterloo, ON N2L 3G1, Canada (e-mail: ishan_mishra@g.harvard.edu).

Color versions of one or more of the figures in this paper are available online at http://ieeexplore.ieee.org.

Digital Object Identifier 10.1109/JSTQE.2016.2616447

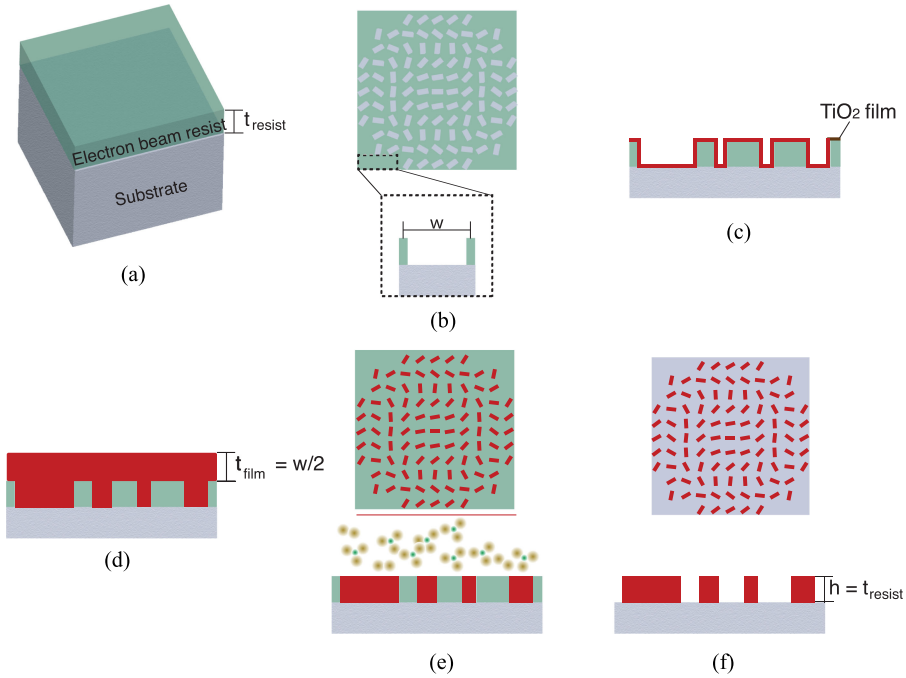

Fig. 1. Schematic illustrating fabrication steps of a titanium dioxide (TiO_2) metasurface. (a) A glass substrate is first spin-coated with electron beam lithography (EBL) resist (ZEP 520 A). (b) The resist is exposed by EBL and is subsequently developed in 99% o-xylene. (c) and (d) Atomic layer deposition (ALD) is used to deposit TiO_2 onto the patterned resist. (e) Due to the conformal deposition of ALD, which results in a blanket TiO_2 layer on top of the resist, we etch down the TiO_2 until the resist layer is reached. (f) The resist is stripped by an overnight Remover-PG bath. The heights of the nanostructures are defined by the height of the spin-coated resist [112].

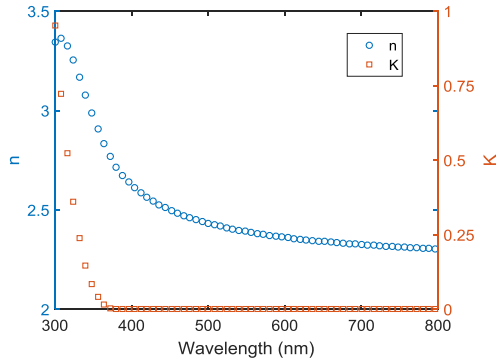

Fig. 2. Extracted real (n) and imaginary (K) parts of the refractive index of TiO_2 from ellipsometry measurements on a thin film layer of TiO_2 deposited on a silicon substrate [112].

lenses [36], [47]–[67], waveplates [68]–[73], mirrors [74]–[76], beam deflectors and gratings [77]–[85], holograms [86]–[96], and polarization sensitive [56], [65], [73], [97]–[111] devices have been demonstrated using this concept. In this paper, we concentrate on metalenses due to their widespread applications in various optical systems including imaging, spectroscopy, laser fabrication, as well as the general lack of compelling experimental results that explicitly demonstrate these metalenses can actually possess capabilities on-par with their traditional counterparts.

This paper is organized as follows. In Section II, we discuss the fabrication approach for building a metasurface platform that operates efficiently at visible wavelengths. In Section III, we report on metalenses designed using the Pancharatnam-

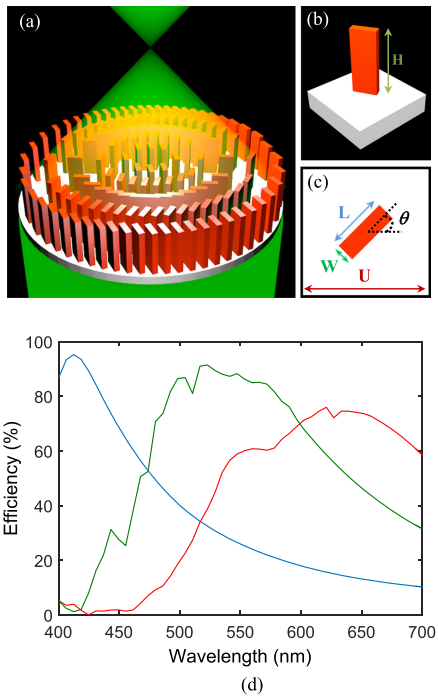

Fig. 3. (a) Schematic of a transmissive metalens consisting of an array of TiO_2 nanofins on a glass substrate. (b) Side-view of the building block of the metalens: a single nanofin, showing its height. (c) Top-view of the nanofin with width W, length L, angle θ and the unit cell lattice constant U. (d) Simulated conversion efficiency for three design wavelengths as a function of wavelength. Optimized parameters for the design wavelength of 405 nm (532 nm; 660 nm) are $H = 600$ nm, $W = 40$ nm, $L = 150$ nm and $U = 200$ nm ($H = 600$ nm, $W = 95$ nm, $L = 250$ nm and $U = 325$ nm; $H = 600$ nm, $W = 85$ nm, $L = 410$ nm and $U = 430$ nm) [62].

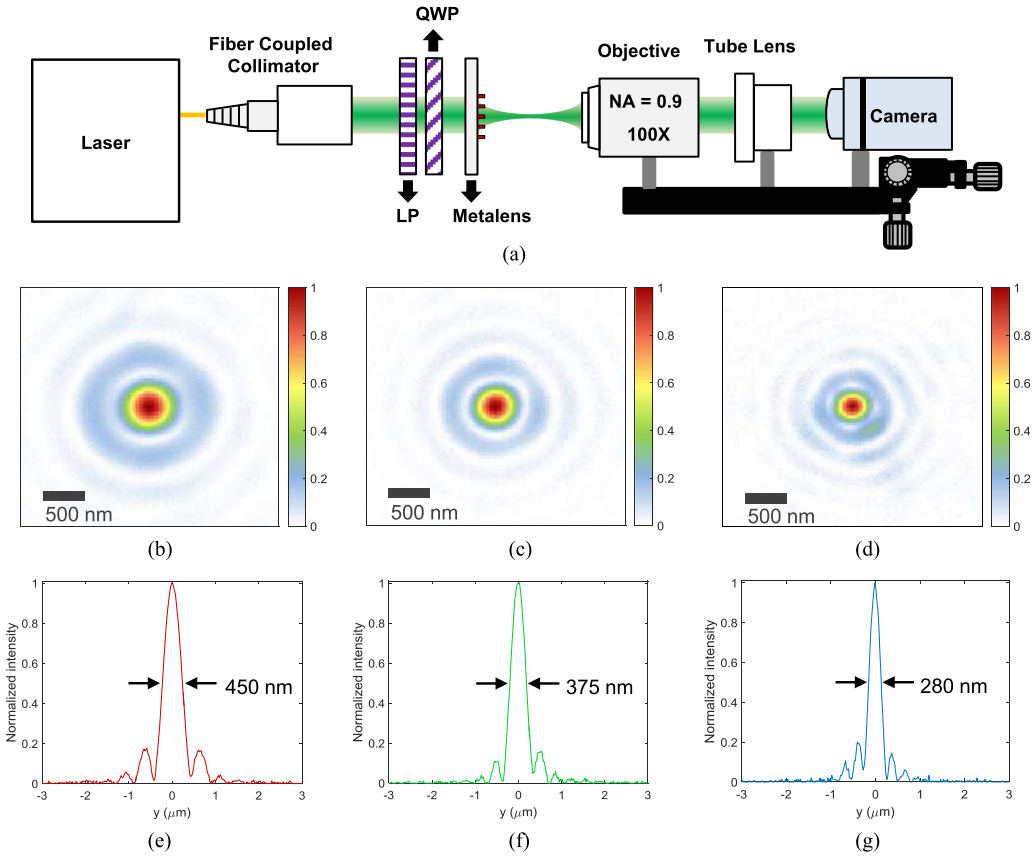

Fig. 4. (a) Schematic of the set-up used to characterize the metalenses. A laser beam is collimated by a fiber-coupled collimator and passed through a linear polarizer (LP) and quarter-waveplate (QWP) to generate circularly polarized light. After interaction with the metalens, the focal spot is captured by an objective paired with a tube lens to form an image on a CMOS camera. (b)–(d) Measured focal spots of three metalenses designed at the wavelengths (b) 660 nm, (c) 532 nm and (d) 405 nm. (e)–(g) Corresponding vertical cuts of the focal spots shown in (b)–(d) [62].

Berry (geometric) phase. We present their diffraction-limited focusing and high resolution imaging capabilities. Section IV illustrates how one can utilize the circular polarization sensitivity (arising from the geometric phase) of these metalenses to realize chiral metalenses. Finally, in Section V, we demonstrate polarization *insensitive* metalenses with high efficiency and numerical apertures.

II. Metasurface Platform for Visible Spectrum

As with any other optical component, the efficiency of a metasurface is one of the key factors that underlie its usefulness for practical applications. Highly efficient silicon-based [45], [50], [54], [58], [59], [61], [63], [77], [93], [97]–[101], [108], [113]–[115] and plasmonic [23], [73], [78], [81], [92] metasurfaces have been demonstrated mostly in the infrared range, using well-established silicon and plasmonic nano-antenna fabrication technology. The mature fabrication technology of silicon enables high aspect-ratio SWS with precise control over the shape and sidewall-profile as well as with negligible surface roughness, all of which are necessary to accurately control the wavefront of incident light. On the other hand, plasmonic nano-antennas, due to their strong interactions with light, only require subwavelength thicknesses which greatly simplifies their fabrication process. Typically, a straightforward lift-off process, without a dry-etching step is adequate. However, neither of these metasurface approaches can be adapted for efficient operation in the visible spectrum because of intrinsic absorption loss of the materials used: silicon, gold and silver (or other noble metals). Although lossless dielectrics in the visible spectrum such as titanium dioxide [6], [7], quartz [116] and silicon nitride [117] are viable alternatives to overcome this problem, due to the subwavelength and high aspect-ratio requirements of dielectric SWS, the fabrication becomes very challenging. Any deviation in the shape and geometry of these building blocks introduces unwanted phase and amplitude modulation, which in turn degrades the performance of the metasurface. This has been observed in the recent work of Zhan *et al.* [117]. Despite using lossless SiN in the visible range, the efficiency of the metalens with $\mathrm{NA} = 0.75$ was $\sim$10%, with a measured focal spot size much larger than an ideal diffraction-limited lens [117]. In particular, one major issue associated with the dry-etching of these dielectrics is the inevitable tapering of the sidewalls. This is a long-standing challenge and has been observed in numerous earlier works, such as Lalanne *et al.* [6], [7] where titanium dioxide (TiO_2) was etched to realize diffractive elements. Although a highly efficient blazed grating and lens [6], [7] ($\mathrm{NA} = 0.25$) were achieved at the wavelengths of 633 and 860 nm, respectively, a crucial point to note is that for shorter wavelengths in the visible range (e.g. 400–500 nm) the fabrication constraints become more demanding since required nanostructure sizes scale

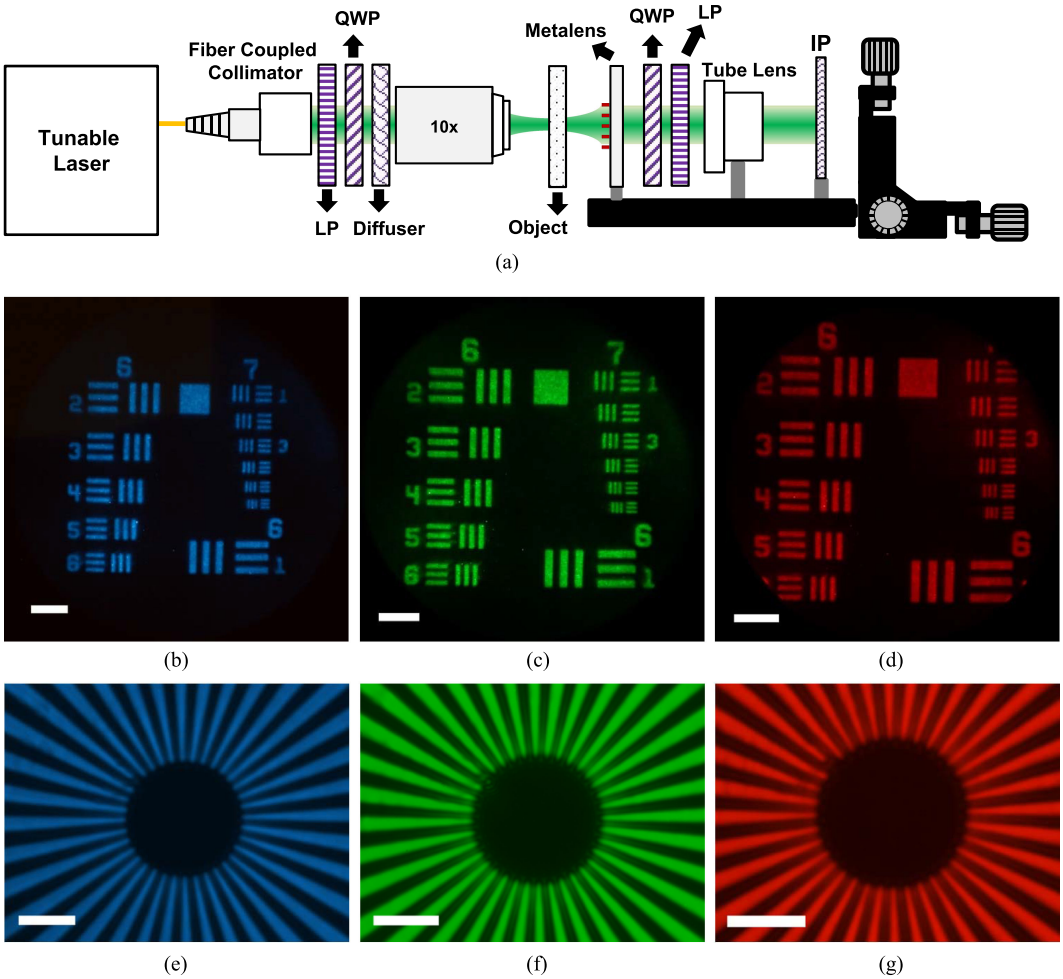

Fig. 5. (a) Schematic of the set-up used for imaging using a metalens. A 10× objective is used to focus the input collimated circularly polarized light to illuminate the test object. The metalens paired with a tube lens forms an image of the object on the image plane (IP). (b)–(d) Images of the 1951 United States Air Force (USAF) resolution test chart formed by the metalens under illumination wavelengths of (b) 480 nm, (c) 550 nm and (d) 620 nm. Scale bar: 40 μm. To capture the image, we placed a translucent screen at the location of the IP. The projected image was captured by a Canon digital single-lens reflex (DSLR) camera. (e)–(g) Images of a Siemens star formed by the metalens under illumination wavelengths of (e) 480 nm, (f) 540 nm, and (g) 620 nm. Scale bar: 10 μm. To capture this image, we placed a color camera at the IP. For all imaging experiments here, the metalens used was designed for $\lambda_d = 532$ nm, with diameter of 2 mm, and focal length $f = 725$ μm [62].

down with the wavelength. We have recently developed a fabrication method [112] that specifically avoids dry-etching in order to define the geometry of these SWS. Instead, as shown in Fig. 1, we use a process similar to lift-off in which the geometry of the SWS is determined by the electron beam lithography (EBL) resist. After EBL and development, TiO_2 is deposited by atomic later deposition (ALD) [112], [118]. Due to the conformal coating of ALD, the deposited film completely fills the gap defined by the resist. Note that one only needs to deposit TiO_2 as thick as half of the maximum width (w/2) of the SWS in order to achieve a given height H, which is determined by the thickness of resist. This is an essential time-saving step and makes this fabrication process practical and scalable. Moreover, the benefits of using TiO_2 are two-fold: it possesses negligible optical absorption in the visible spectrum and a relatively large refractive index (see Fig. 2). The latter ensures strong optical confinement to provide the required phase coverage and increase packing density for high focusing efficiency; the former is necessary to minimize optical losses.

III. Metalenses Based on Geometric Phase

A. Design Principle

In order to realize a high performance transmissive metalens [see Fig. 3(a)], each SWS should impart the required phase ($\varphi(x, y) = \frac{2\pi}{\lambda_d}(f - \sqrt{x^2 + y^2 + f^2})$, λ_d: design wavelength, f: focal length) at a given coordinate (x, y) with maximum transmission efficiency [62]. In this section, we consider a TiO_2 nanofin as the SWS [see Fig. 3(b)]. Under circularly polarized (CP) incident light, the required phase is realized by using the geometric phase approach [58], [86], [92]. The nanofin is designed as a half-wave plate utilizing structural birefringence (the effective index is different for two orthogonal linear polarizations: along the nanofin width and length [see Fig. 3(c)], so that it converts the handedness of incident CP light and simultaneously imparts a geometric phase equal to twice its rotation angle [see Fig. 3(c)]. The conversion is maximized by adjusting their width, length and height [see Fig. 3(b) and (c)]. Fig. 3(d) shows that a conversion efficiency as high as 95% can be achieved and

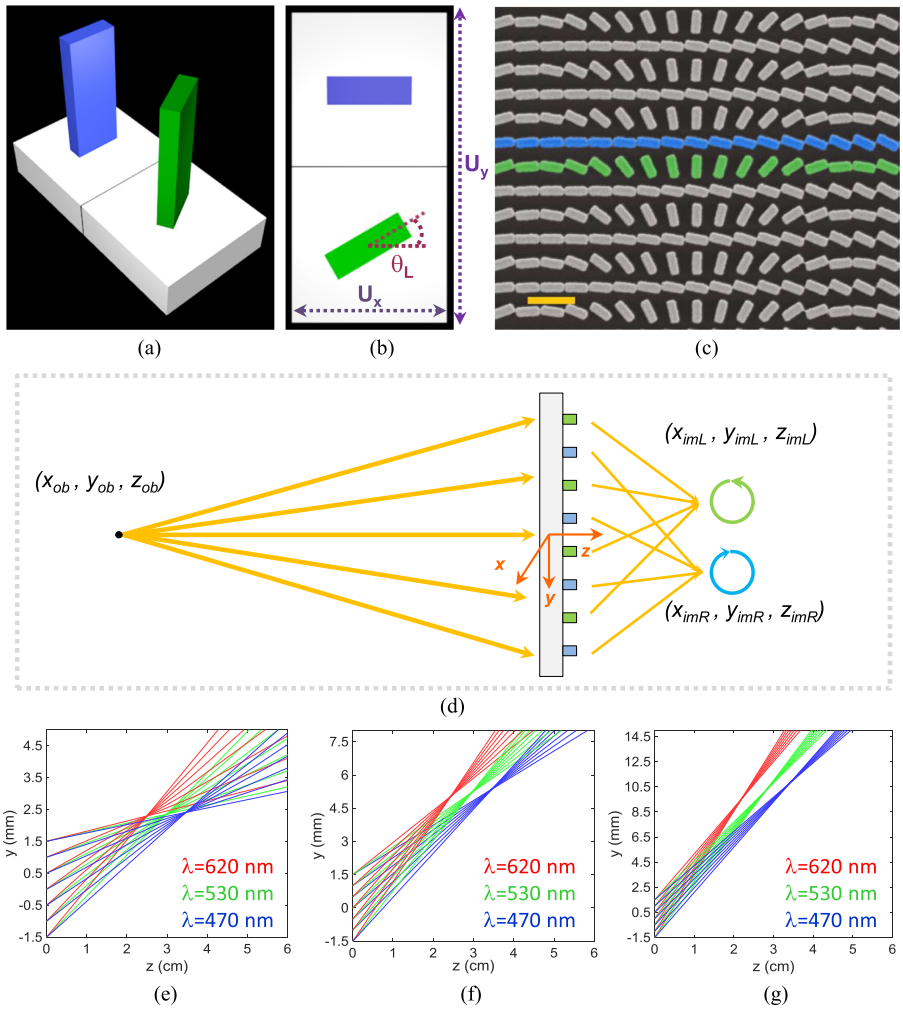

Fig. 6. (a) The building block of the chiral metalens (CML) comprises of two nanofins on a glass substrate. (b) Top-view of the nanofins: $\mathrm{U}_x = 300$ nm and $U_y = 600$ nm. The nanofins in blue and green impart the required phase to focus right-circularly polarized (RCP) light and left-circularly polarized (LCP) light, respectively. (c) Top-view scanning electron microscope (SEM) image of a portion of the fabricated CML. For ease of visualization, the two interlaced arrays of nanofins are false-colored. The CML has a diameter of 3 mm. Scale bar: 600 nm. (d) Schematic representation of the imaging principle behind the CML. The CML forms two images of an object, located at coordinates ($x_{\mathrm{ob}} = 0$, $y_{\mathrm{ob}} = 0$, $z_{\mathrm{ob}} = -18$ cm), at (x_{imL}, y_{imL}, z_{imL}) and (x_{imR}, y_{imR}, z_{imR}), corresponding to LCP and RCP components of incident light. The coordinate values are wavelength dependent because of the dispersive design of the CML. These values are $x_{\mathrm{imL}} = 2.34$ mm, $y_{\mathrm{imL}} = -0.184$ mm, $z_{\mathrm{imL}} = 29.90$ mm, $x_{\mathrm{imR}} = 2.34$ mm, $y_{\mathrm{imR}} = 0.184$ mm and $z_{\mathrm{imR}} = 29.90$ mm at the design wavelength of 530 nm. (e)–(g) Simulations based on ray-tracing illustrating the engineered dispersive response of the CML. The focusing angles are (e) 4.5°, (f) 10° and (g) 20° [65].

the peak is tunable across the visible spectrum by appropriately adjusting the building block parameters.

B. Characterization and Imaging

We designed and fabricated three metalenses at wavelengths of 405, 532 and 660 nm. All metalenses have a diameter of 240 μm and focal length of 90 μm, yielding a $\mathrm{NA} = 0.8$. The performances of these metalenses were characterized using a custom-built microscope. A schematic of the measurement set-up is shown in Fig. 4(a), which consists of a fiber-coupled laser source connected to a reflective collimator. The collimated beam is then passed through a linear polarizer and quarter-waveplate to generate CP light. An objective (Olympus, $100\times$, $\mathrm{NA} = 0.9$) is paired with a tube lens ($f = 180$ mm) to capture the light after interaction with the metalens and to form an image on a CMOS camera (Edmund EO-5012). To characterize the focal spots of the metalenses, we used laser sources with linewidths less than 100 MHz (Ondax Inc.). For efficiency measurements, a tunable laser (SuperK, NTK Photonics) was used and the CMOS camera was replaced by a photodetector (Thorlabs S120C). The efficiency is defined as the ratio of the optical power of the focused beam to the optical power of the incident beam. The latter was measured as the optical power passing through a circular aperture (aluminum on glass) with the same diameter as the metalenses. The focal spots are measured and shown in Fig. 4(b)–(d). Highly symmetric focal spots were achieved for all three metalenses. This is more clearly evidenced by the intensity cuts along the focal spots, as shown in Fig. 4(e)–(g). Most importantly, the obtained focal spot sizes are close to the ideal diffraction-limited values. This is an essential factor for many applications beyond microscopy such as laser fabrication/lithography and machine vision where the focal spot size

defines the achievable resolution. It also sets the limit for the maximum imaging resolution when these metalenses are used for imaging purposes. Full-width at half-maxima (FWHM) of 450, 375, and 280 nm, with corresponding focusing efficiencies of 66%, 73% and 86% were measured for these metalenses at their design wavelengths of 660, 532 and 405 nm, respectively.

To test their use in monochromatic imaging, we fabricated a new metalens designed at the wavelength $\lambda_d = 532\ \mathrm{nm}$ with a diameter of 2 mm and focal length of 725 μm. Fig. 5(a) shows the schematic of the imaging set-up, which is modified compared to the one shown in Fig. 4(a). Here, a Mitutoyo objective ($10\times$) is placed after the LP, QWP and diffuser; it was used to provide intensified illumination on the object. The diffuser is used to reduce laser speckles. The metalens is paired with a tube lens ($f = 100\ \mathrm{mm}$) to form an image of the test object (1951 United States Air Force (USAF) resolution test) on a translucent screen. Finally, the image was captured with a Canon digital single-lens reflex (DSLR) camera. We used the translucent screen with the DSLR camera since the size of the image was bigger than the CMOS camera chip. Fig. 5(b)–(d) shows the images at illumination wavelengths of 480, 550 and 620 nm. All features including the smallest bars (width of 2.2 μm with center-to-center distance of 4.4 μm) are well resolved. We repeated this imaging experiment with a different object (Siemens star). Here the minimum center-to-center distance between two neighboring bars at the center is $\sim$1.7 μm and is well resolved across the visible wavelengths [see Fig. 5(e)–(g)]. For this experiment, we placed a color camera on the image plane (IP) to capture the image. Because the focal length of the metalens varies with wavelength, for each illumination wavelength, the distance between the object and the metalens is adjusted to bring the object to focus. In other words, the focal length decreases as wavelength increases, resulting in larger magnification for $\lambda = 620\ \mathrm{nm}$ ($167\times$) than for $\lambda = 480\ \mathrm{nm}$ ($124\times$).

IV. Chiral Metalens

Chirality is a fascinating part of the natural world and has been widely observed from the microscopic (e.g. amino acids) to the macroscopic scale (e.g. certain species of snails and beetles [119], [120]). The vast majority of biochemical compounds ranging from sweeteners to pharmaceutical drugs possess chirality. For example, aspartame, an artificial sweetener, is a chiral molecule where one enantiomer tastes sweet and the other bitter. While the chirality of aspartame affects its taste, in drugs, the consequences can be much more severe. As a result, the ability to distinguish the chirality of an object is essential. Current spectroscopy and imaging techniques employ multiple, cascaded optical components in complex setups to extract chiral information. In this context, metasurfaces with the ability to control the wavefront and polarization of light without requiring volumetric propagation offer significant potential to realize multifunctional devices in an ultra-thin and compact configuration. In this section, we demonstrate a planar metalens that can simultaneously resolve chiral and spectral information of an object without the requirement of additional optical components such as polarizers, waveplates or even gratings.

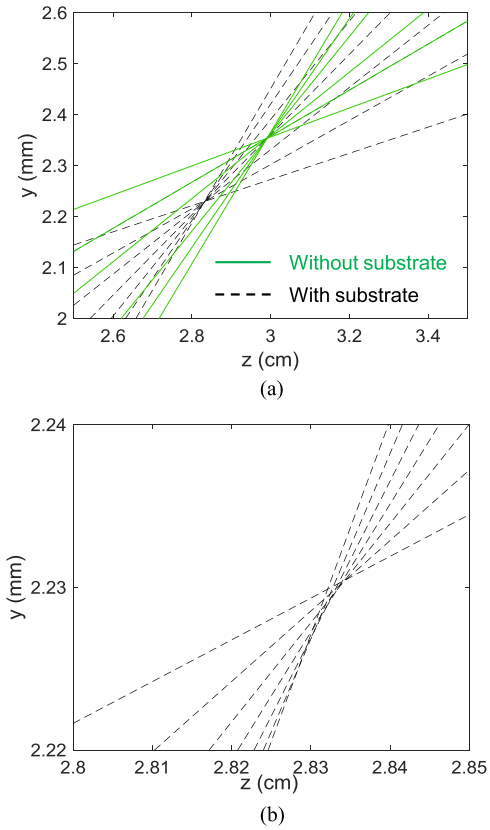

Fig. 7. Ray-tracing simulations showing the effect of substrate. The phase profile of the chiral metalens is calculated without taking into account the optical path through the substrate. (a) The optical path difference due to the substrate results in a slight reduction of the focal length. (b) Zoomed-in view of the simulation of the focal spot (with substrate) depicting slight broadening of the focal spot by a few microns, which is in the order of our camera pixel size 4.54 μm [65].

A. Design Principle

In the previous section, we have demonstrated highly efficient metalenses in the visible range using the geometric phase approach. This requires CP incident light with a specific helicity. In other words, such a metalens focuses one helicity of light while defocusing the opposite one. This arises from the fact that the sign of the phase imparted by each nanofin reverses upon switching the helicity of incident light. Here, we utilize this feature to realize a chiral metalens (CML). Fig. 6(a) and (b) show the building block of the CML consisting of two nanofins on a glass substrate. While the nanofin (located at (x_R, y_R, z_R)) colored in blue imparts the required phase to focus the right-circularly polarized (RCP) light, for left-circularly polarized (LCP) incident light this is achieved by the nanofin (located at $(x_L,\ y_L,\ z_L)$ in green. In order to spatially separate these two focal spots, the CML is designed with an off-axis focusing scheme [see Fig. 6(d)]. We consider a point-to-point (finite conjugate) imaging configuration [see Fig. 6(d)] and LCP incident light to extract the required phase of the CML design. We set the center ($x = 0, y = 0, z = 0$) of the CML as the reference point; therefore the reference path (f) is the distance between the object and the image through the reference point:

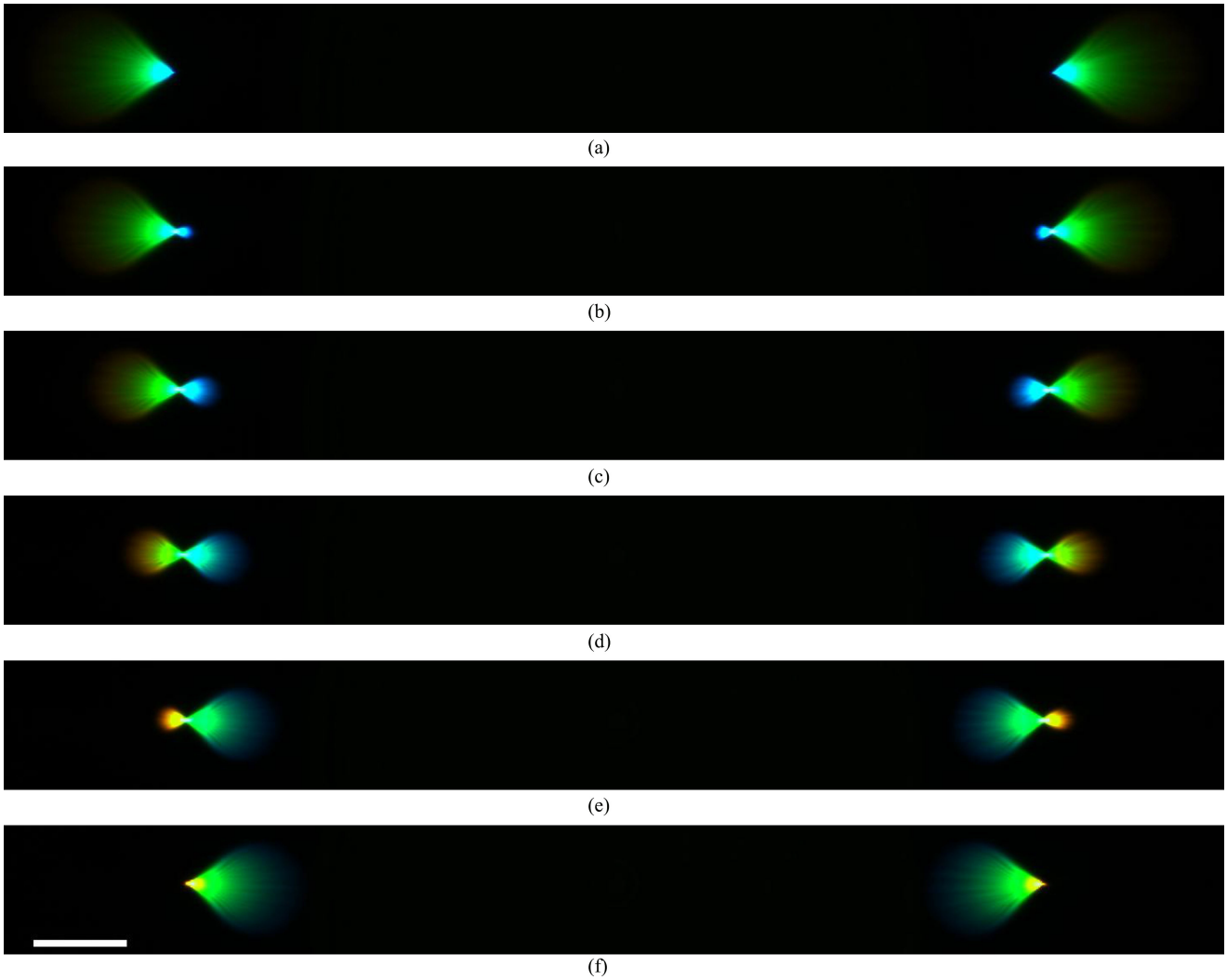

Fig. 8. Dispersive response of the chiral metalens (CML). (a)–(f) The CML forms a rainbow-like image of the fiber. The fiber was connected to a tunable laser with center wavelength of 500 nm and bandwidth of 100 nm. Input polarization state was set to linear by placing a linear polarizer between the CML and the fiber. The camera distance from the CML was adjusted from (a) to (f) in order to selectively focus a specific wavelength. For all images, scale bar is 0.5 mm [65].

$$\begin{aligned} f &= f_1 + f_2 \\ f_1 &= \sqrt{{x_{\mathrm{ob}}}^2 + {y_{\mathrm{ob}}}^2 + {z_{\mathrm{ob}}}^2} \\ f_2 &= \sqrt{{x_{\mathrm{imL}}}^2 + {y_{\mathrm{imL}}}^2 + {z_{\mathrm{imL}}}^2} \end{aligned} \tag{1}$$

We assume the object (located at $(x_{\mathrm{ob}},\ y_{\mathrm{ob}},\ z_{\mathrm{ob}})$) to be a point source with linear polarization, i.e. the superposition of equal amplitudes of RCP and LCP components. We first consider the LCP component of the point source. The optical path difference between object and image $(x_{\mathrm{imL}},\ y_{\mathrm{imL}},\ z_{\mathrm{imL}})$ through the nanofin at the position $(x_L,\ y_L,\ z_L)$ and the reference path results in a phase delay:

$$\varphi_d\left(x_L,\ y_L, z_L\right) = \frac{2\pi}{\lambda_d}\left(\Delta D_{\mathrm{ob}} + \Delta D_{\mathrm{im}} - f\right) \tag{2}$$

where $\lambda_d = 530$ nm is the design wavelength and ΔD_{ob} and ΔD_{im} are distances between the nanofin and the object and nanofin and the image, respectively. These distances can be calculated by:

$$\begin{aligned} \Delta D_{\mathrm{ob}} &= \sqrt{\left(x_L - x_{\mathrm{ob}}\right)^2 + \left(y_L - y_{\mathrm{ob}}\right)^2 + \left(z_L - z_{\mathrm{ob}}\right)^2} \\ \Delta D_{\mathrm{im}} &= \sqrt{\left(x_L - x_{\mathrm{imL}}\right)^2 + \left(y_L - y_{\mathrm{imL}}\right)^2 + \left(z_L - z_{\mathrm{imL}}\right)^2} \end{aligned} \tag{3}$$

In order to achieve constructive interference between the optical path through the nanofin and the reference point, this phase difference $\varphi_d(x_L,\ y_L,\ z_L)$ must be compensated by the nanofin located at $(x_L,\ y_L,\ z_L)$. Therefore, the rotation angle of this nanofin must be set to:

$$\theta_L\left(x_L,\ y_L, z_L\right) = \frac{\varphi_d\left(x_L,\ y_L,\ z_L\right)}{2} \tag{4}$$

For the RCP component, a similar derivation can be carried out resulting a rotation of the nanofin at (x_R, y_R, z_R):

$$\theta_R\left(x_R,\ y_R,\ \ z_R\right) = -\frac{\varphi_d\left(x_R,\ \ y_R,\ \ z_R\right)}{2} \tag{5}$$

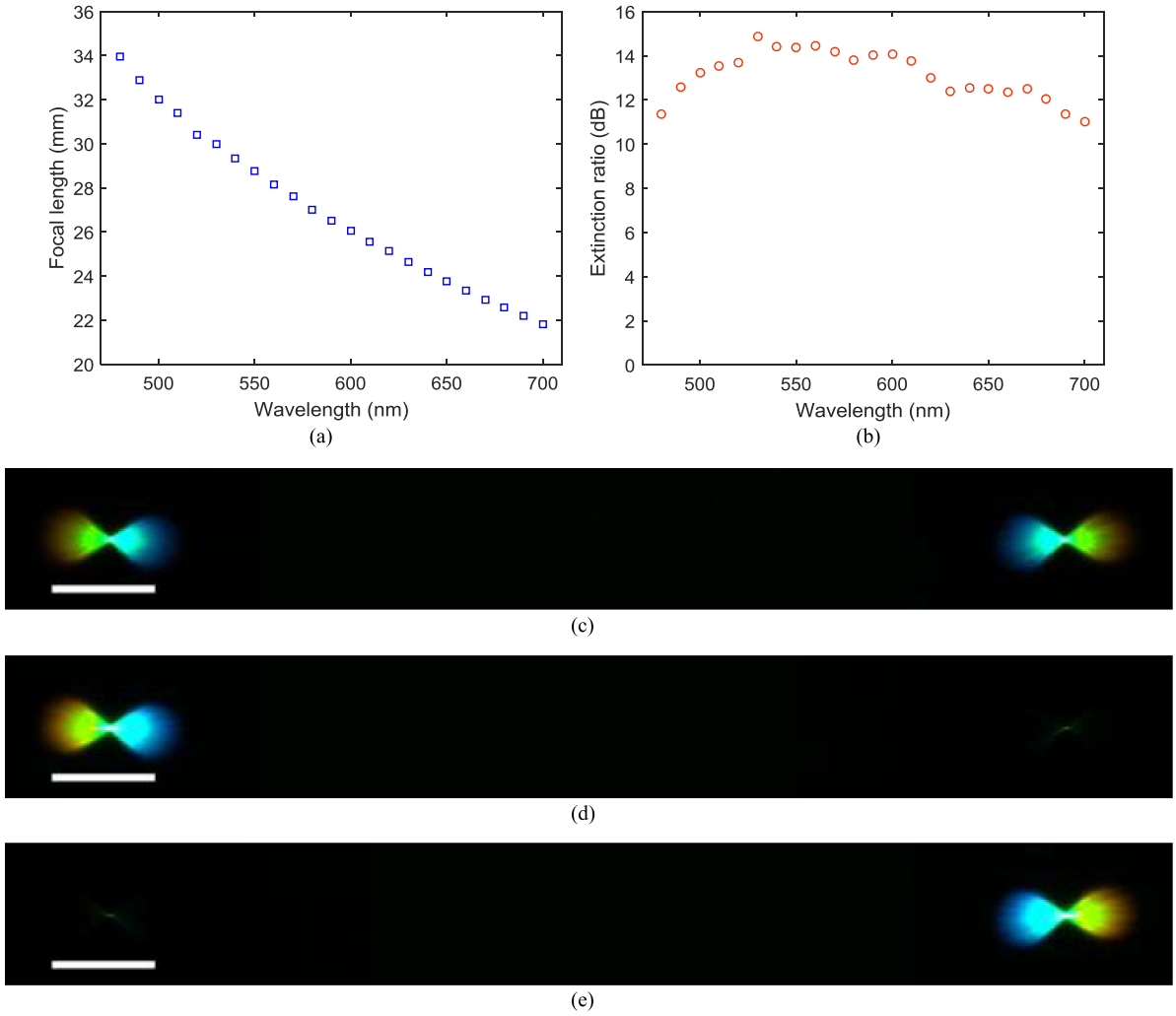

Fig. 9. (a) Measured focal length (f_2) of the chiral metalens (CML) as a function of wavelength. (b) Measured extinction ratio of the CML versus wavelength. (c) The CML forms two images of the object (a facet of single mode fiber) within the field-of-view of a color camera. The fiber emits broadband light linearly polarized by a polarizer. (d) Images formed by the CML when the polarization of the emitting light is switched to left-circular polarization. (e) Images formed by the CML when the polarization of the emitting light is switched to right-circular polarization. The gain and exposure time of the camera were kept fixed for (c)–(e). All images were captured while the camera was saturated at the focal point, which allows for visualization of the out-of-focus colors. The scale bar is 0.5 mm for (c)–(e) [65].

Here, we do not take into account the effects of the substrate when calculating the phase difference. This in principle results in aberrations of focal spot as shown in Fig. 7. The ray-tracing simulation shows slight broadening of the focal spot, about a few microns. This broadening is comparable to our camera pixel size 4.54 μm; therefore, as we will show later, its effect on the image quality is negligible.

By utilizing the engineered dispersion associated with the off-axis focusing while taking into account the intrinsic dispersion of the CML design, one can also extract spectral information [65]. The reciprocal linear dispersion $(\frac{\Delta\lambda}{\Delta r})$ of the CML can be simplified to (for $\Delta\alpha \ll \alpha$):

$$\frac{\Delta\lambda}{\Delta r} = \frac{\Delta\lambda}{f_2 \cdot \Delta\alpha}$$

$$\Delta\alpha = \sin^{-1}\left[\left(1 + \frac{\Delta\lambda}{\lambda_d}\right) \cdot \sin(\alpha)\right] - \alpha \tag{6}$$

where $\Delta\alpha$ is the change in the off-axis focusing angle α due to the change in the wavelength ($\Delta\lambda$). This dispersion can be engineered by appropriately selecting the focal length f_2 and focusing angle α. Fig. 6(e)–(g) shows the effect of the focusing angle on the dispersion. As expected, the larger the focusing angle, the greater the dispersion. Using Eq. (6), we can define the spectral resolution of the CML as:

$$\delta\lambda = \frac{\Delta\lambda}{f_2 \cdot \Delta\alpha} \cdot \frac{0.61\lambda_d}{NA} \tag{7}$$

where *NA* is the numerical aperture of the off-axis CML defined in [52]. We assume a hypothetical CML with a diameter of 3 mm and focal length $f_2 = 3$ cm, and find theoretical spectral resolutions of 4.5, 2 and 1 nm for focusing angles of 4.5°, 10° and 20°, respectively. For simplicity, the change of focal length with changing wavelength, which can further affect the spectral resolution, is not taken into account.

B. Chiral Imaging

The scanning electron microscope (SEM) image of the fabricated CML is shown in Fig. 6(c). The CML design param-

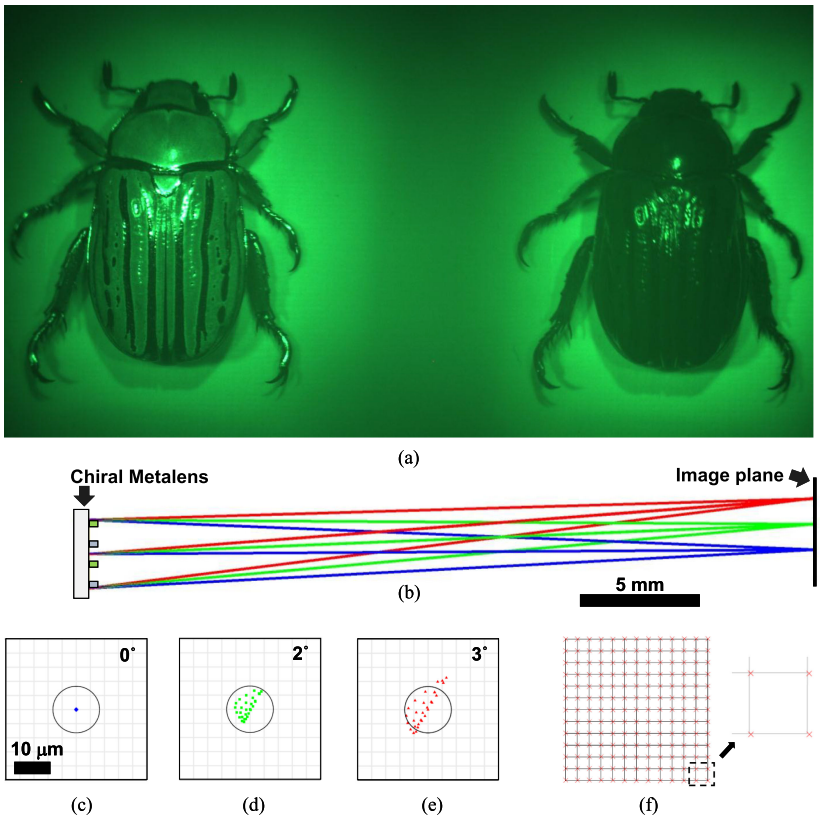

Fig. 10. (a) The chiral metalens (CML) forms two images of the beetle, *Chrysina gloriosa*, within the same field-of-view of a color camera. Two green LEDs paired with 10 nm bandpass filter centered at 532 nm were used for illumination. (b)–(f) Ray-tracing analysis using Zemax at wavelength $\lambda = 530\,\mathrm{nm}$, considering the effect of a 0.5-mm-thick fused silica substrate. The beams originate from point sources on the left side of the CML (not shown here), and are then focused by the CML onto the image plane. (b) Ray-tracing diagram illustrating the case of a laterally displaced point source 0° (blue), 2° (green) and 3° (red) relative to the normal of the CML. (c)–(e) Spot diagrams showing the intersection points on the image plane with respect to their chief rays. The black circle shows the size of the diffraction-limited Airy disk. (f) A plot of grid distortion. The red crosses show the intercept points of chief rays on the image plane. The distance from a cross to its nearest black corner represents image distortion [65].

eters are as follows: CML diameter of 3 mm, $f_1 = 18\,\mathrm{cm}$, $f_2 = 3\,\mathrm{cm}$ and $\alpha = 4.5°$. To demonstrate the multispectral and chiral capability of the CML, we first used a facet of a single mode fiber as the object. The fiber was connected to a tunable laser (Superk, NKT Photonics) with the center wavelength and bandwidth set to 550 and 100 nm, respectively. Fig. 8 shows how the CML simultaneously focuses and disperses the beam resulting in the formation of a rainbow-like image. The CML focuses a certain color on the camera whereas others are out of focus, which is a direct result of its wavelength-dependent focal length [see Fig. 9(a)]. However, as shown in Fig. 8(a)–(f) one can selectively focus onto a desired wavelength by adjusting the camera position. By looking at Fig. 8 from (a) to (f), we note that the lateral displacement in the position of the focal spot for different wavelengths originates from the dispersion engineering of the design.

We then examined the polarization response of the CML. For a linearly polarized incident beam, the CML forms two identical images within the camera's field-of-view [see Fig. 9(c)]. Upon changing the incident polarization state to LCP, we observed that the image on the right fades with a simultaneous increase in the intensity of the image on the left [see Fig. 9(d)]. By switching the helicity of incident beam, an opposite effect was seen [see Fig. 9(e)]. This chiral feature of the CML is quantified by measuring the extinction ratio (ER), which is defined as the ratio of intensity of the LCP (RCP) image to that of the RCP (LCP) image under LCP (RCP) illumination. Due to imperfections of the quarter waveplate used in the experiment, we adopted the method of Azzam and Lopez [121] to measure the ER. A high ER of 15 dB was measured as shown in Fig. 9(b).

Next, for the imaging of a chiral macroscopic object with complex features, we chose *Chrysina gloriosa*, a beetle known to possess strong natural circular dichroism (CD) [119], [120]. We placed the beetle 18 cm away from the CML and situated the color camera ∼3 cm on the other side of the CML. Illumination was provided by two green LEDs paired with bandpass filters with a center wavelength of 532 nm and bandwidth of 10 nm. These filters were used to reduce the LEDs bandwidth and thus mitigate chromatic aberrations. As shown in Fig. 10(a), the CML forms two images of the beetle on the camera chip with opposite helicity. The large contrast between two images is a manifestation of the strong CD of the beetle. This is expected since the beetle's exoskeleton reflects LCP light while absorbing more of RCP light [119], [120]. It is evident from Fig. 10(a) that there are no obvious aberrations in the image of the beetle. To quantify this, we performed a simulation using a commercially available ray-tracing software (OpticsStudio, Zemax Inc.). The required phase profile was calculated by bringing all the rays emitted from an on-axis point source at 18 cm away from the CML to a 4.5° off-axis point 3 cm away on the image plane depicted in Fig. 10(b). The blue rays of Fig. 10(b) shows the

(a)

(b)

(c)

Fig. 11. (a) and (b) Images formed by the chiral metalens (CML) under (a) blue (b) red LEDs illumination. Blue LEDs were paired with 10 nm bandpass filters centered at 488 nm; red LEDs were paired with10 nm bandpass filters centered at 620 nm. (c) Images of a one-dollar coin formed by the CML under green LED illumination. Green LEDs were paired with 10 nm bandpass filters centered at 532 nm [65].

simulated results for the wavelength $\lambda = 530\ \mathrm{nm}$. The rays between the point source and CML are not plotted for ease of visualization. The green and red rays represent the same wavelength but after lateral displacement of the point source on the object plane 2° and 3° degrees with respect to the center of the CML, respectively. This is to quantify the performance of the CML for an extended object where object points are

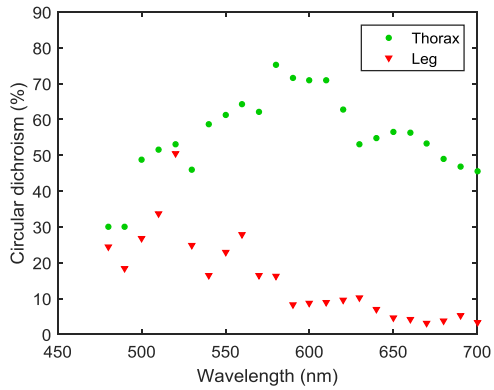

Fig. 12. Circular dichroism from two different parts of the beetle's exoskeleton as a function of wavelength.

located off the optical axis. Fig. 10(c)–(e) shows the intersected points on the image plane with respect to their chief rays, i.e. the ray that passes through the center of CML. The black circle shows the region enclosed by a diffraction-limited Airy disk. The spread of the intersection points shown in Fig. 10(c)–(e) thus represents aberrations, which reduce the performance of the optical system. However, since the camera used has a pixel size $\sim 4.54\ \mu$m, a slight spreading of the focal spot does not significantly reduce the image quality because it only causes one or two pixels of blurring. Another crucial aberration that might occur is distortion resulting from the nonlinear displacement of the image points. This can be quantified by Fig. 10(f) for the case of a 6-degree field-of-view. The 6 degree field-of-view corresponds to an area of about $2 \times 2\ \mathrm{cm}^2$ on the object plane which is larger than the size of the beetle. The black grid shows ideal imaging without distortion and the coordinates of each intersected point are defined as $(x_{\mathrm{ideal}},\ y_{\mathrm{ideal}})$. The red crosses show the intersected points $(x_{\mathrm{real}},\ y_{\mathrm{real}})$ on the image plane for the chief ray emitted within the $2 \times 2\ \mathrm{cm}^2$ area. The percentage of distortion is defined by:

$$\sqrt{\frac{(x_{\mathrm{Ideal}} - x_{\mathrm{Real}})^2 + (y_{\mathrm{Ideal}} - y_{\mathrm{Real}})^2}{x_{\mathrm{Ideal}}^2 + y_{\mathrm{Ideal}}^2}} \times 100\ \% \qquad (8)$$

In our case, the distortion is $\sim 0.5\%$, which ensures the high quality image replication of the beetle.

Although the CML is designed for 530 nm, it is still capable of performing imaging with high quality at other wavelengths across the visible range. The images of the beetle formed by the CML under blue and red LEDs illumination are shown in Fig. 11(a) and (b). Compared to Fig. 10(a), a slight background noise is evident. This background partially comes from the fact that the efficiency of the CML drops at red and blue wavelengths, in addition to the reduced reflectivity of the beetle in these wavelength ranges.

As a control experiment, we also imaged an achiral object, a United States one-dollar coin. Fig. 11(c) shows that the CML forms two nearly identical images. We also demonstrate the capability to locally measure the CD of different parts of the beetle's exoskeleton. We first focused a laser beam (SuperK, NKT Photonics) with a bandwidth of 10 nm onto the beetle's

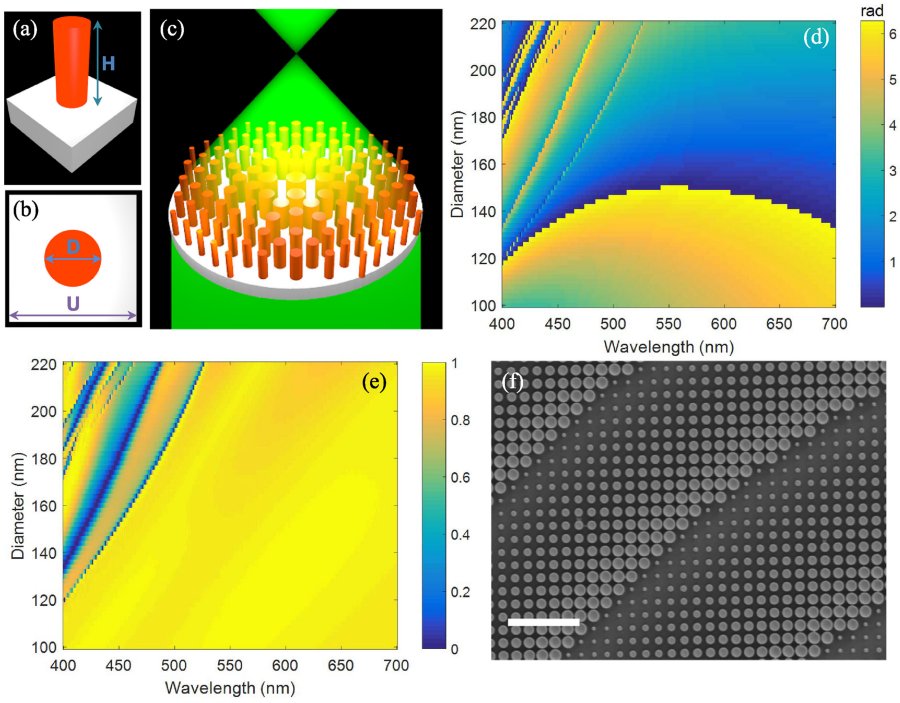

Fig. 13. (a) and (b) Side (a) and top (b) views of a polarization-insensitive metalens' (PIML) building block: a TiO_2 nanopillar on a glass substrate. The nanopillars are arranged in a square lattice. Optimized parameters for PIMLs at design wavelength $\lambda_d = 405$ nm ($\lambda_d = 532$ nm; $\lambda_d = 660$ nm) are as follows: $U = 180$ nm ($U = 250$ nm; $U = 350$ nm), $H = 400$ nm ($H = 600$ nm; $H = 600$ nm) and the nanopillar diameters D varies between 80 to 155 nm (100 nm $< D <$ 220 nm; 100 nm $< D <$ 320 nm). (c) Schematic of the PIML consisting of an array of nanopillars. (d) Simulated phase map for the PIML designed at $\lambda_d = 532$ nm. Each point on this phase map represents a relative phase difference between a nanopillar with diameter D and a reference point. The reference point is the one where there is no nanopillar. (e) Simulated transmission map for the PIML designed at $\lambda_d = 532$ nm. (f) Top-view scanning electron microscope image of a portion of a fabricated PIML. Scale bar: 2 μm.

thorax. The diameter of the focal spot was ~ 100 μm to avoid any permanent damage to the exoskeleton. The CML collects the reflected light and forms two spots on the camera. These two spots have different intensities corresponding to the two circularly polarized states (RCP:I_R and LCP:I_L). We obtained the CD $(\frac{I_L - I_R}{I_L + I_R})$ as a function of the wavelength by capturing images. We repeated this CD measurement on the beetle's leg. Fig. 12 shows large CD values of the beetle peaking in the green region of the spectrum, as expected [119], [120].

In this study, we used the CML to characterize the CD of a beetle, but our approach can be also utilized to examine the chirality of a wide range of objects. Ultimately, one of the main factors that determine the spatial resolution of the CML is its NA. Here, in order to image a large object, we chose a long focal length resulting in low NA, which also allows for increasing the field-of-view and having more tolerance in aberrations. One can readily improve the imaging resolution by reducing the focal length or increasing the diameter of the CML.

V. Polarization Insensitive Metalens

So far, we have demonstrated metalenses using the geometric phase approach. These metalenses require CP light and this feature was subsequently exploited to realize a multi-spectral chiral metalens. However, for many practical applications, polarization-insensitive planar lenses are required. In this section, we discuss the experimental realization of high NA metalenses operating in transmission mode in the visible range under arbitrary polarized illumination.

A. Design and Fabrication

To overcome the polarization dependence of phase, we used TiO_2 nanopillars as shown in Fig. 13(a) and (b). Because of their circular cross-section, the phase implementation is independent of polarization, resulting in a polarization-insensitive metalens (PIML). The required phase is achieved via the waveguiding effect by controlling the nanopillar diameter for a fixed height. A schematic of the PIML is shown in Fig. 13(c). At position (x, y), a nanopillar with diameter $D(x, y)$ imparts the required phase given by:

$$\varphi_t(x, y) = \frac{2\pi}{\lambda_d}\left(f - \sqrt{x^2 + y^2 + f^2}\right) \tag{9}$$

In order to determine the required diameter of nanopillars at every position, we performed finite difference time domain (FDTD from Lumerical Inc.) simulations. To ensure high efficiency, other nanopillar parameters including height H and unit cell size U are also optimized for. The heights of the nanopillars must be sufficiently tall to ensure 2π phase coverage over attainable diameters. Our fabrication process sets the lower limit on the diameter while the unit cell size defines the upper limit. The design wavelength and NA determine the maximum size of the unit cell. To meet the Nyquist criterion, the unit cell size of the lens must be smaller than $\frac{\lambda}{2 \cdot NA}$. Fig. 13(d) and (e) show the phase $\varphi(D)$ and transmission $T(D)$ maps as a

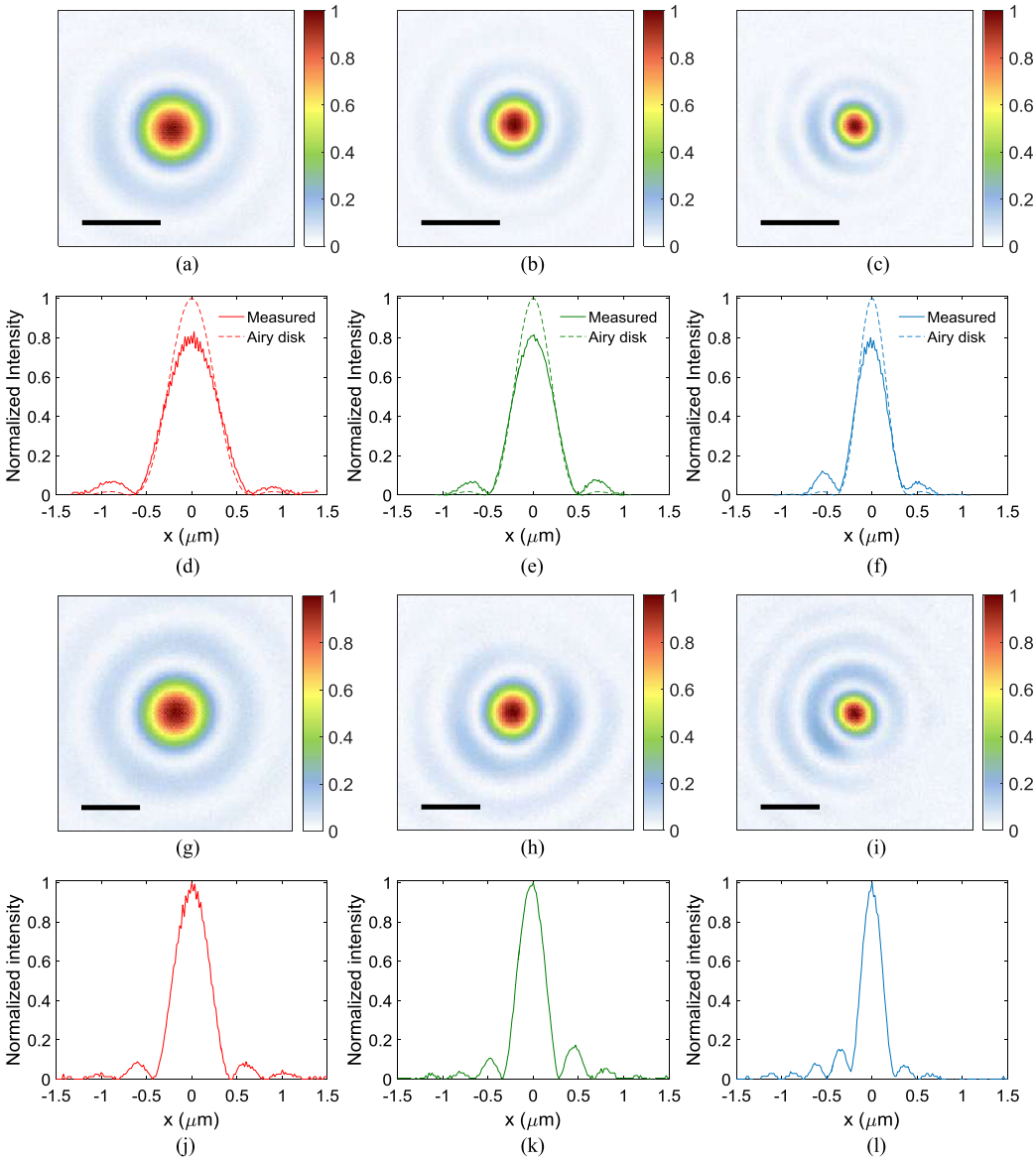

Fig. 14. (a)–(c) Measured focal spots of the polarization-insensitive metalenses (PIML) at their design wavelengths of (a) 660 nm, (b) 532 nm and (c) 405 nm respectively. Scale bar: 1 μm. (d)–(f) Corresponding horizontal cuts of focal spots shown in (a)–(c). An ideal intensity cross-section of an Airy disk is overlaid onto each horizontal cut. All results shown in (a)–(f) are from PIMLs with focal lengths of 200 μm, diameters of 300 μm and numerical apertures $\mathrm{NA} = 0.6$. (g)–(i) Measured focal spots of the PIMLs at their design wavelengths of (a) 660 nm, (b) 532 nm and (c) 405 nm respectively. Scale bar: 500 nm. (j)–(l) Corresponding horizontal cuts of focal spots shown in (g)–(i). All results shown in (g)–(l) are from PIMLs with focal lengths of 90 μm, diameters of 300 μm and numerical apertures $\mathrm{NA} = 0.85$.

function of diameter, respectively, for a PIML with the design wavelength $\lambda_d = 532$ nm. Full phase coverage with high transmission (>87%) is obtained.

We designed PIMLs with NA = 0.60 and $\mathrm{NA} = 0.85$ at three design wavelengths of 405, 532 and 660 nm. We discretized the phase mask $\varphi_t(x_i,\ y_j)$ of each PIML at its design wavelengths by assuming square lattice unit cells with dimensions $U \times U$. At each position $(x_i,\ y_j)$, we select an appropriate diameter in order to minimize the following quantity:

$$\left| T_m e^{i\varphi_t(x_i,\ y_j)} - T(D)\, e^{i\varphi(D)} \right| \tag{10}$$

where T_m is the transmission averaged over all the diameters, and $T(D)$ and $\varphi(D)$ are the transmission and phase of a nanopillar with a diameter *D*, respectively.

B. Characterization

A SEM image of a fabricated PIML is shown in Fig. 13(f). We measured the focal spots of the three PIMLs with $\mathrm{NA} = 0.6$. A similar set-up to that shown in Fig. 4(a) was used, except for the removal of the linear polarizer and the quarter-waveplate and replacement of the objective with an Olympus with $\mathrm{NA} = 0.95$. Focal spot profiles and their corresponding horizontal cuts are shown in Fig. 14(a)–(c) and Fig. 14(d)–(f), respectively. Based on these measurement results, we also calculated the Strehl ratio. The Strehl ratio can have a value between 0 and 1. For an ideal lens with a diffraction limited focal spot and intensity distribution of an Airy disk, this value is unity. We calculate the Strehl ratio by normalizing the peak intensity of each measured horizontal cut such that it has the same area under the curve

as an ideal Airy function, which has a maximum intensity of unity and diffraction-limited $FWHM = 0.514\frac{\lambda_d}{NA}$. Strehl ratios of 0.8, 0.82 and 0.83 are obtained for PIMLs designed at wavelengths of 405, 532 and 660 nm, respectively. For comparison, Strehl ratios of 0.81, 0.84 and 0.81 for the vertical cuts at the above wavelengths are achieved. These values are close to those obtained from the horizontal cuts, revealing the symmetry of the focal spots. In addition, these PIMLs have measured efficiencies of 30%, 70% and 90% at their design wavelengths of 405, 532 and 660 nm. For shorter wavelength PIMLs have lower efficiencies than the metalenses based on geometric phase because the required variation in the diameter of the nanopillars to obtain the phase profile is subject to fabrication imperfections mostly associated with the proximity effect during the ebeam lithography process. We also fabricated PIMLs with a higher $\mathrm{NA} = 0.85$ designed at wavelengths of 405, 532 and 660 nm and achieved corresponding efficiencies of efficiency of 33%, 60% and 60%. Fig. 14(g)–(i) show the focal spots of the three PIMLs at their design wavelengths. Highly symmetric focal spots with diffraction-limited sizes are obtained. For PIMLs at their design wavelengths of 405, 532 and 660 nm, the FWHMs of the horizontal cuts of their focal spots are 259, 327 and 424 nm, respectively. These values are very close to those obtained from the corresponding vertical cuts: 256, 344, 428 nm. For these PIMLs, Strehl ratios of 0.76 (0.78), 0.82 (0.84) and 0.85 (0.85) were obtained from the measured horizontal (vertical) cuts corresponding to design wavelengths of 405, 532 and 660 nm. Large values of Strehl ratios together with diffraction-limited focusing reaffirm the high quality of fabrication and capability of this TiO_2-based platform to realize high performance monochromatic polarization-insensitive planar lenses in the visible spectrum.

VI. Conclusion

In this paper, we have demonstrated a dielectric-based platform to realize high performance metasurfaces in the visible spectrum. The use of ALD and EBL ensures high aspect-ratio nanostructures with vertical sidewalls and precise control over other geometrical parameters. This is essential for effective control of the phase of incident light and eventually the wavefront. Using this platform, we have reported both polarization-sensitive and polarization-insensitive metalenses. While the polarization sensitivity of the former was utilized to demonstrate chiral imaging, planar lenses that operate under any polarization are in high demand for many applications. These polarization insensitive planar lenses have been shown to possess high NAs with efficiency up to 90%. Their thickness is less than a micron and can focus incident light to a spot as small as 0.64λ. Their limited bandwidth of operation can be expanded to a multi-wavelength regime via dispersion engineering of the phase shifting-element [59], [66] and with further optimizations potentially to a continuous wavelength range. The latter is an essential step for integration of these metalenses into applications such as camera modules in cellphones, laptops and professional photographic cameras.

Acknowledgment

The authors thank E. Hu for the supercontinuum laser (NKT "SuperK").

References

[1] S. Wang, M. Moharam, R. Magnusson, and J. Bagby, "Guided-mode resonances in planar dielectric-layer diffraction gratings," *J. Opt. Soc. Amer. A*, vol. 7, pp. 1470–1474, 1990.
[2] W. Stork, N. Streibl, H. Haidner, and P. Kipfer, "Artificial distributed-index media fabricated by zero-order gratings," *Opt. Lett.*, vol. 16, pp. 1921–1923, 1991.
[3] M. W. Farn, "Binary gratings with increased efficiency," *Appl. Opt.*, vol. 31, pp. 4453–4458, 1992.
[4] P. Kipfer *et al.*, "Infrared optical components based on a microrelief structure," *Opt. Eng.*, vol. 33, pp. 79–84, 1994.
[5] P. Lalanne, "Waveguiding in blazed-binary diffractive elements," *J. Opt. Soc. Amer. A*, vol. 16, pp. 2517–2520, 1999.
[6] P. Lalanne, S. Astilean, P. Chavel, E. Cambril, and H. Launois, "Design and fabrication of blazed binary diffractive elements with sampling periods smaller than the structural cutoff," *J. Opt. Soc. Amer. A*, vol. 16, pp. 1143–1156, 1999.
[7] M.-S. L. Lee *et al.*, "Imaging with blazed-binary diffractive elements," *J. Opt. A: Pure Appl. Opt.*, vol. 4, p. S119–S124, 2002.
[8] U. D. Zeitner *et al.*, "High performance diffraction gratings made by e-beam lithography," *Appl. Phys. A*, vol. 109, pp. 789–796, 2012.
[9] W. E. Kock, "Metallic delay lenses," *Bell Syst. Tech. J.*, vol. 27, pp. 58–82, 1948.
[10] F. T. Chen and H. G. Craighead, "Diffractive lens fabricated with mostly zeroth-order gratings," *Opt. Lett.*, vol. 21, pp. 177–179, 1996.
[11] L. d'Auria, J. Huignard, A. Roy, and E. Spitz, "Photolithographic fabrication of thin film lenses," *Opt. Commun.*, vol. 5, pp. 232–235, 1972.
[12] J. B. Pendry, "Negative refraction makes a perfect lens," *Phys. Rev. Lett.*, vol. 85, pp. 3966–3969, 2000.
[13] R. A. Shelby, D. R. Smith, and S. Schultz, "Experimental verification of a negative index of refraction," *Science*, vol. 292, pp. 77–79, 2001.
[14] A. Grbic and G. V. Eleftheriades, "Experimental verification of backward-wave radiation from a negative refractive index metamaterial," *J. Appl. Phys.*, vol. 92, pp. 5930–5935, 2002.
[15] D. R. Smith, J. B. Pendry, and M. C. Wiltshire, "Metamaterials and negative refractive index," *Science*, vol. 305, pp. 788–792, 2004.
[16] V. M. Shalaev *et al.*, "Negative index of refraction in optical metamaterials," *Opt. Lett.*, vol. 30, pp. 3356–3358, 2005.
[17] A. Alù and N. Engheta, "Achieving transparency with plasmonic and metamaterial coatings," *Phys. Rev. E*, vol. 72, 2005, Art. no. 016623.
[18] J. B. Pendry, D. Schurig, and D. R. Smith, "Controlling electromagnetic fields," *Science*, vol. 312, pp. 1780–1782, 2006.
[19] V. M. Shalaev, "Optical negative-index metamaterials," *Nature Photon.*, vol. 1, pp. 41–48, 2007.
[20] C. M. Soukoulis, S. Linden, and M. Wegener, "Negative refractive index at optical wavelengths," *Science*, vol. 315, pp. 47–49, 2007.
[21] J. A. Schuller, R. Zia, T. Taubner, and M. L. Brongersma, "Dielectric metamaterials based on electric and magnetic resonances of silicon carbide particles," *Phys. Rev. Lett.*, vol. 99, 2007, Art. no. 107401.
[22] U. Levy *et al.*, "Inhomogenous dielectric metamaterials with space-variant polarizability," *Phys. Rev. Lett.*, vol. 98, 2007, Art. no. 243901.
[23] J. K. Gansel *et al.*, "Gold helix photonic metamaterial as broadband circular polarizer," *Science*, vol. 325, pp. 1513–1515, 2009.
[24] B. Luk'yanchuk *et al.*, "The fano resonance in plasmonic nanostructures and metamaterials," *Nature Mater.*, vol. 9, pp. 707–715, 2010.
[25] B. Walther *et al.*, "Spatial and spectral light shaping with metamaterials," *Adv. Mater.*, vol. 24, pp. 6300–6304, 2012.
[26] N. Engheta, "Circuits with light at nanoscales: Optical nanocircuits inspired by metamaterials," *Science*, vol. 317, pp. 1698–1702, 2007.
[27] N. Engheta and R. W. Ziolkowski, *Metamaterials: Physics and Engineering Explorations*. New York, NY, USA: Wiley, 2006.
[28] D. Schurig *et al.*, "Metamaterial electromagnetic cloak at microwave frequencies," *Science*, vol. 314, pp. 977–980, 2006.
[29] U. Leonhardt, "Optical conformal mapping," *Science*, vol. 312, pp. 1777–1780, 2006.
[30] W. Cai, U. K. Chettiar, A. V. Kildishev, and V. M. Shalaev, "Optical cloaking with metamaterials," *Nature Photon.*, vol. 1, pp. 224–227, 2007.

[31] L. H. Gabrielli, J. Cardenas, C. B. Poitras, and M. Lipson, "Silicon nanostructure cloak operating at optical frequencies," *Nature Photon.*, vol. 3, pp. 461–463, 2009.

[32] X. Ni, Z. J. Wong, M. Mrejen, Y. Wang, and X. Zhang, "An ultrathin invisibility skin cloak for visible light," *Science*, vol. 349, pp. 1310–1314, 2015.

[33] E. Cubukcu, K. Aydin, E. Ozbay, S. Foteinopoulou, and C. Soukoulis, "Subwavelength resolution in a two-dimensional photonic-crystal-based superlens," *Phys. Rev. Lett.*, vol. 91, 2003, Art. no. 207401.

[34] N. Fang, H. Lee, C. Sun, and X. Zhang, "Sub-diffraction-limited optical imaging with a silver superlens," *Science*, vol. 308, pp. 534–537, 2005.

[35] Z. Liu, H. Lee, Y. Xiong, C. Sun, and X. Zhang, "Far-field optical hyperlens magnifying sub-diffraction-limited objects," *Science*, vol. 315, pp. 1686–1686, 2007.

[36] A. Grbic, L. Jiang, and R. Merlin, "Near-field plates: Subdiffraction focusing with patterned surfaces," *Science*, vol. 320, pp. 511–513, 2008.

[37] S. Kawata, Y. Inouye, and P. Verma, "Plasmonics for near-field nano-imaging and superlensing," *Nature Photon.*, vol. 3, pp. 388–394, 2009.

[38] S. Sun *et al.*, "Gradient-index meta-surfaces as a bridge linking propagating waves and surface waves," *Nature Mater.*, vol. 11, pp. 426–431, 2012.

[39] F. Falcone *et al.*, "Babinet principle applied to the design of metasurfaces and metamaterials," *Phys. Rev. Lett.*, vol. 93, 2004, Art. no. 197401.

[40] N. Yu *et al.*, "Light propagation with phase discontinuities: Generalized laws of reflection and refraction," *Science*, vol. 334, pp. 333–337, 2011.

[41] A. V. Kildishev, A. Boltasseva, and V. M. Shalaev, "Planar photonics with metasurfaces," *Science*, vol. 339, 2013, Art. no. 1232009.

[42] N. Yu and F. Capasso, "Flat optics with designer metasurfaces," *Nature Mater.*, vol. 13, pp. 139–150, 2014.

[43] N. I. Zheludev and Y. S. Kivshar, "From metamaterials to metadevices," *Nature Mater.*, vol. 11, pp. 917–924, 2012.

[44] S. B. Glybovski, S. A. Tretyakov, P. A. Belov, Y. S. Kivshar, and C. R. Simovski, "Metasurfaces: From microwaves to visible," *Phys. Rep.*, vol. 634, pp. 1–72, 2016.

[45] S. Jahani and Z. Jacob, "All-dielectric metamaterials," *Nature Nanotechnol.*, vol. 11, pp. 23–36, 2016.

[46] T. Zentgraf, J. Valentine, N. Tapia, J. Li, and X. Zhang, "An optical "Janus" device for integrated photonics," *Adv. Mater.*, vol. 22, pp. 2561–2564, 2010.

[47] L. Verslegers *et al.*, "Planar lenses based on nanoscale slit arrays in a metallic film," *Nano Lett.*, vol. 9, pp. 235–238, 2008.

[48] F. M. Huang, T. S. Kao, V. A. Fedotov, Y. Chen, and N. I. Zheludev, "Nanohole array as a lens," *Nano Lett.*, vol. 8, pp. 2469–2472, 2008.

[49] G. M. Lerman, A. Yanai, and U. Levy, "Demonstration of nanofocusing by the use of plasmonic lens illuminated with radially polarized light," *Nano Lett.*, vol. 9, pp. 2139–2143, 2009.

[50] D. Fattal, J. Li, Z. Peng, M. Fiorentino, and R. G. Beausoleil, "Flat dielectric grating reflectors with focusing abilities," *Nature Photon.*, vol. 4, pp. 466–470, 2010.

[51] F. Lu, F. G. Sedgwick, V. Karagodsky, C. Chase, and C. J. Chang-Hasnain, "Planar high-numerical-aperture low-loss focusing reflectors and lenses using subwavelength high contrast gratings," *Opt. Express*, vol. 18, pp. 12606–12614, 2010.

[52] F. Aieta *et al.*, "Aberration-free ultrathin flat lenses and axicons at telecom wavelengths based on plasmonic metasurfaces," *Nano Lett.*, vol. 12, pp. 4932–4936, 2012.

[53] E. T. Rogers *et al.*, "A super-oscillatory lens optical microscope for subwavelength imaging," *Nature Mater.*, vol. 11, pp. 432–435, 2012.

[54] S. Vo *et al.*, "Sub-wavelength grating lenses with a twist," *IEEE Photon. Technol. Lett.*, vol. 26, no. 13, pp. 1375–1378, Jul. 2014.

[55] Q. Wang *et al.*, "Optically reconfigurable metasurfaces and photonic devices based on phase change materials," *Nature Photon.*, vol. 10, pp. 60–65, 2016.

[56] X. Chen *et al.*, "Dual-polarity plasmonic metalens for visible light," *Nature Commun.*, vol. 3, 2012, Art. no. 1198.

[57] A. Pors, M. G. Nielsen, R. L. Eriksen, and S. I. Bozhevolnyi, "Broadband focusing flat mirrors based on plasmonic gradient metasurfaces," *Nano Lett.*, vol. 13, pp. 829–834, 2013.

[58] D. Lin, P. Fan, E. Hasman, and M. L. Brongersma, "Dielectric gradient metasurface optical elements," *Science*, vol. 345, pp. 298–302, 2014.

[59] F. Aieta, M. A. Kats, P. Genevet, and F. Capasso, "Multiwavelength achromatic metasurfaces by dispersive phase compensation," *Science*, vol. 347, pp. 1342–1345, 2015.

[60] J. Cheng, D. Ansari-Oghol-Beig, and H. Mosallaei, "Wave manipulation with designer dielectric metasurfaces," *Opt. Lett.*, vol. 39, pp. 6285–6288, 2014.

[61] A. Arbabi, Y. Horie, A. J. Ball, M. Bagheri, and A. Faraon, "Subwavelength-thick lenses with high numerical apertures and large efficiency based on high-contrast transmitarrays," *Nature Commun.*, vol. 6, pp. 1–6, 2015.

[62] M. Khorasaninejad *et al.*, "Metalenses at visible wavelengths: Diffraction-limited focusing and subwavelength resolution imaging," *Science*, vol. 352, pp. 1190–1194, 2016.

[63] M. Khorasaninejad, W. T. Chen, J. Oh, and F. Capasso, "Super-dispersive off-axis meta-lenses for compact high resolution spectroscopy," *Nano Lett.*, vol. 16, pp. 3732–3737, 2016.

[64] F. Monticone, N. M. Estakhri, and A. Alù, "Full control of nanoscale optical transmission with a composite metascreen," *Phys. Rev. Lett.*, vol. 110, 2013, Art. no. 203903.

[65] M. Khorasaninejad *et al.*, "Multispectral chiral imaging with a metalens," *Nano Lett.*, vol. 16, pp. 4595–4600, 2016.

[66] M. Khorasaninejad *et al.*, "Achromatic metasurface lens at telecommunication wavelengths," *Nano Lett.*, vol. 15, pp. 5358–5362, 2015.

[67] E. Arbabi, A. Arbabi, S. M. Kamali, Y. Horie, and A. Faraon, "Multiwavelength polarization-insensitive lenses based on dielectric metasurfaces with meta-molecules," *Optica*, vol. 3, pp. 628–633, 2016.

[68] R. Gordon *et al.*, "Strong polarization in the optical transmission through elliptical nanohole arrays," *Phys. Rev. Lett.*, vol. 92, 2004, Art. no. 037401.

[69] P. Biagioni *et al.*, "Near-field polarization shaping by a near-resonant plasmonic cross antenna," *Phys. Rev. B*, vol. 80, 2009, Art. no. 153409.

[70] Y. Zhao and A. Alù, "Manipulating light polarization with ultrathin plasmonic metasurfaces," *Phys. Rev. B*, vol. 84, 2011, Art. no. 205428.

[71] N. Yu *et al.*, "A broadband, background-free quarter-wave plate based on plasmonic metasurfaces," *Nano Lett.*, vol. 12, pp. 6328–6333, 2012.

[72] T. Ellenbogen, K. Seo, and K. B. Crozier, "Chromatic plasmonic polarizers for active visible color filtering and polarimetry," *Nano Lett.*, vol. 12, pp. 1026–1031, 2012.

[73] Y. Zhao, M. Belkin, and A. Alù, "Twisted optical metamaterials for planarized ultrathin broadband circular polarizers," *Nature Commun.*, vol. 3, 2012, Art. no. 870.

[74] C. F. Mateus, M. C. Huang, Y. Deng, A. R. Neureuther, and C. J. Chang-Hasnain, "Ultrabroadband mirror using low-index cladded subwavelength grating," *IEEE Photon. Technol. Lett.*, vol. 16, no. 2, pp. 518–520, Feb. 2004.

[75] L. Chen, M. C. Huang, C. F. Mateus, C. J. Chang-Hasnain, and Y. Suzuki, "Fabrication and design of an integrable subwavelength ultrabroadband dielectric mirror," *Appl. Phys. Lett.*, vol. 88, 2006, Art. no. 031102.

[76] F. Aieta, P. Genevet, M. Kats, and F. Capasso, "Aberrations of flat lenses and aplanatic metasurfaces," *Opt. Express*, vol. 21, pp. 31530–31539, 2013.

[77] C. J. Chang-Hasnain, "High-contrast gratings as a new platform for integrated optoelectronics," *Semicond. Sci. Technol.*, vol. 26, 2010, Art. no. 014043.

[78] S. Sun *et al.*, "High-efficiency broadband anomalous reflection by gradient meta-surfaces," *Nano Lett.*, vol. 12, pp. 6223–6229, 2012.

[79] X. Ni, N. K. Emani, A. V. Kildishev, A. Boltasseva, and V. M. Shalaev, "Broadband light bending with plasmonic nanoantennas," *Science*, vol. 335, p. 427, 2012.

[80] P. P. Iyer, M. Pendharkar, and J. A. Schuller, "Electrically reconfigurable metasurfaces using heterojunction resonators," *Adv. Opt. Mater.*, vol. 4, pp. 1582–1588, 2016.

[81] Z. Li, E. Palacios, S. Butun, and K. Aydin, "Visible-frequency metasurfaces for broadband anomalous reflection and high-efficiency spectrum splitting," *Nano Lett.*, vol. 15, pp. 1615–1621, 2015.

[82] Y. H. Fu, A. I. Kuznetsov, A. E. Miroshnichenko, Y. F. Yu, and B. Luk'yanchuk, "Directional visible light scattering by silicon nanoparticles," *Nature Commun.*, vol. 4, 2013, Art. no. 1527.

[83] A. I. Kuznetsov, A. E. Miroshnichenko, Y. H. Fu, J. Zhang, and B. Luk'Yanchuk, "Magnetic light," *Sci. Rep.*, vol. 2, 2012, Art. no. 492.

[84] Y. F. Yu *et al.*, "High-transmission dielectric metasurface with 2π phase control at visible wavelengths," *Laser Photon. Rev.*, vol. 9, pp. 412–418, 2015.

[85] F. Qin *et al.*, "Hybrid bilayer plasmonic metasurface efficiently manipulates visible light," *Sci. Adv.*, vol. 2, 2016, Art. no. e1501168.

[86] U. Levy, H.-C. Kim, C.-H. Tsai, and Y. Fainman, "Near-infrared demonstration of computer-generated holograms implemented by using subwavelength gratings with space-variant orientation," *Opt. Lett.*, vol. 30, pp. 2089–2091, 2005.
[87] M. Ozaki, J.-i. Kato, and S. Kawata, "Surface-plasmon holography with white-light illumination," *Science*, vol. 332, pp. 218–220, 2011.
[88] S. Larouche, Y.-J. Tsai, T. Tyler, N. M. Jokerst, and D. R. Smith, "Infrared metamaterial phase holograms," *Nature Mater.*, vol. 11, pp. 450–454, 2012.
[89] W. T. Chen *et al.*, "High-efficiency broadband meta-hologram with polarization-controlled dual images," *Nano Lett.*, vol. 14, pp. 225–230, 2013.
[90] L. Huang *et al.*, "Three-dimensional optical holography using a plasmonic metasurface," *Nature Commun.*, vol. 4, 2013, Art. no. 2808.
[91] X. Ni, A. V. Kildishev, and V. M. Shalaev, "Metasurface holograms for visible light," *Nature Commun.*, vol. 4, 2013, Art. no. 2807.
[92] G. Zheng *et al.*, "Metasurface holograms reaching 80% efficiency," *Nature Nanotechnol.*, vol. 10, pp. 308–312, 2015.
[93] M. Khorasaninejad, A. Ambrosio, P. Kanhaiya, and F. Capasso, "Broadband and chiral binary dielectric meta-holograms," *Sci. Adv.*, vol. 2, 2016, Art. no. e1501258.
[94] D. Wen *et al.*, "Helicity multiplexed broadband metasurface holograms," *Nature Commun.*, vol. 6, 2015, Art. no. 8241.
[95] W. T. Chen *et al.*, "Integrated plasmonic metasurfaces for spectropolarimetry," *Nanotechnology*, vol. 27, 2016, Art. no. 224002.
[96] K. Huang *et al.*, "Silicon multi-meta-holograms for the broadband visible light," *Laser Photon. Rev.*, vol. 10, pp. 500–509, 2016.
[97] Y. Yang *et al.*, "Dielectric meta-reflectarray for broadband linear polarization conversion and optical vortex generation," *Nano Lett.*, vol. 14, pp. 1394–1399, 2014.
[98] M. Khorasaninejad and F. Capasso, "Broadband multifunctional efficient meta-gratings based on dielectric waveguide phase shifters," *Nano Lett.*, vol. 15, pp. 6709–6715, 2015.
[99] M. Khorasaninejad and K. B. Crozier, "Silicon nanofin grating as a miniature chirality-distinguishing beam-splitter," *Nature Commun.*, vol. 5, 2014, Art. no. 5386.
[100] M. Khorasaninejad, W. Zhu, and K. Crozier, "Efficient polarization beam splitter pixels based on a dielectric metasurface," *Optica*, vol. 2, pp. 376–382, 2015.
[101] A. Arbabi, Y. Horie, M. Bagheri, and A. Faraon, "Dielectric metasurfaces for complete control of phase and polarization with subwavelength spatial resolution and high transmission," *Nature Nanotechnol.*, vol. 10, pp. 937–943, 2015.
[102] C. Wu *et al.*, "Spectrally selective chiral silicon metasurfaces based on infrared fano resonances," *Nature Commun.*, vol. 5, 2014, Art. no. 3892.
[103] R. C. Devlin *et al.*, "Spin-to-orbital angular momentum conversion in dielectric metasurfaces," arXiv preprint arXiv:1605.03899, 2016.
[104] E. Maguid *et al.*, "Photonic spin-controlled multifunctional shared-aperture antenna array," *Science*, vol. 352, pp. 1202–1206, 2016.
[105] X. Yin, Z. Ye, J. Rho, Y. Wang, and X. Zhang, "Photonic spin Hall effect at metasurfaces," *Science*, vol. 339, pp. 1405–1407, 2013.
[106] A. Pors, M. G. Nielsen, and S. I. Bozhevolnyi, "Plasmonic metagratings for simultaneous determination of Stokes parameters," *Optica*, vol. 2, pp. 716–723, 2015.
[107] J. Lin *et al.*, "Polarization-controlled tunable directional coupling of surface plasmon polaritons," *Science*, vol. 340, pp. 331–334, 2013.
[108] Z. Bomzon, G. Biener, V. Kleiner, and E. Hasman, "Radially and azimuthally polarized beams generated by space-variant dielectric subwavelength gratings," *Opt. Lett.*, vol. 27, pp. 285–287, 2002.
[109] E. Plum, V. Fedotov, and N. Zheludev, "Extrinsic electromagnetic chirality in metamaterials," *J. Opt. A: Pure Appl. Opt.*, vol. 11, 2009, Art. no. 074009.
[110] E. Plum *et al.*, "Metamaterials: Optical activity without chirality," *Phys. Rev. Lett.*, vol. 102, 2009, Art. no. 113902.
[111] U. Levy, C.-H. Tsai, L. Pang, and Y. Fainman, "Engineering space-variant inhomogeneous media for polarization control," *Opt. Lett.*, vol. 29, pp. 1718–1720, 2004.
[112] R. C. Devlin, M. Khorasaninejad, W. T. Chen, J. Oh, and F. Capasso, "High efficiency dielectric metasurfaces at visible wavelengths," *Proc. Nat. Acad. Sci. USA*, vol. 113, pp. 10473–10478, 2016.
[113] M. Decker *et al.*, "High-efficiency dielectric Huygens' surfaces," *Adv. Opt. Mater.*, vol. 3, pp. 813–820, 2015.
[114] K. E. Chong *et al.*, "Polarization-independent silicon metadevices for efficient optical wavefront control," *Nano Lett.*, vol. 15, pp. 5369–5374, 2015.
[115] P. Spinelli, M. Verschuuren, and A. Polman, "Broadband omnidirectional antireflection coating based on subwavelength surface Mie resonators," *Nature Commun.*, vol. 3, 2012, Art. no. 692.
[116] F. Chen and H. Craighead, "Diffractive phase elements based on two-dimensional artificial dielectrics," *Opt. Lett.*, vol. 20, pp. 121–123, 1995.
[117] A. Zhan *et al.*, "Low-contrast dielectric metasurface optics," *ACS Photon.*, vol. 3, pp. 209–214, 2016.
[118] A. A. High *et al.*, "Visible-frequency hyperbolic metasurface," *Nature*, vol. 522, pp. 192–196, 2015.
[119] V. Sharma, M. Crne, J. O. Park, and M. Srinivasarao, "Structural origin of circularly polarized iridescence in jeweled beetles," *Science*, vol. 325, pp. 449–451, 2009.
[120] M. Srinivasarao, "Nano-optics in the biological world: Beetles, butterflies, birds, and moths," *Chem. Rev.*, vol. 99, pp. 1935–1962, 1999.
[121] R. Azzam and A. G. Lopez, "Accurate calibration of the four-detector photopolarimeter with imperfect polarizing optical elements," *J. Opt. Soc. Amer. A*, vol. 6, pp. 1513–1521, 1989.

Mohammadreza Khorasaninejad received the M.Sc. (Hons.) degree from Amirkabir University of Technology, Tehran, Iran, in 2008, and the Ph.D. degree from the University of Waterloo, Waterloo, Canada, in 2012, both in electrical engineering.

He is currently a Research Associate at Harvard John A. Paulson School of Engineering and Applied Sciences, Cambridge, USA. His research interests include nanophotonics and nanooptics. His work is focused on dielectric metasurfaces.

Dr. Khorasaninejad is a member of the Optical Society of America.

Wei Ting Chen received the B.S. degree in applied physics from the National University of Kaohsiung, Kaohsiung, Taiwan, in 2008, and the Ph.D. degree with Dean's Award in applied physics from Nation Taiwan University, Taipei, Taiwan, in 2014.

In 2012, he was a Visiting Student in the Optoelectronics Research Centre at the University of Southampton, Southampton, U.K. From 2008 to 2009, he was the President of SPIE National Taiwan University Student Chapter. He is currently a Postdoctoral Fellow at Harvard John A. Paulson School of Engineering and Applied Sciences, Harvard University, Cambridge, USA. He is the author of one book chapter and more than 25 journal articles. His research interests include metasurfaces and plasmonics.

Alexander Y. Zhu graduated summa cum laude from the University of Pennsylvania with degrees in material science, mathematics, and physics, and is currently working toward the Ph.D. degree at Harvard University. He has worked on numerous projects related to nanophotonics, plasmonics, and 2-D materials. He is supported by a National Science Scholarship from the Agency of Science, Technology and Research, Singapore.

Jaewon Oh was born in Seoul, South Korea, in 1995. He is currently working toward the B.A.Sc. degree in nanotechnology engineering at the University of Waterloo, ON, Canada.

From 2014 to 2016, he has been an Undergraduate Research Assistant at the University of Waterloo and at Harvard John A. Paulson School of Engineering and Applied Sciences, Harvard University, Cambridge, MA. His research interests include quantum phenomena in photosynthesis, optical engineering with metasurfaces, and metabolic engineering with CRISPR interference.

Robert C. Devlin received the B.S. and M.S. degrees in electrical engineering and materials science and engineering from Drexel University, Philadelphia. He graduated summa cum laude. He is currently working toward the Ph.D. degree in applied physics at Harvard John A. Paulson School of Engineering and Applied Sciences, Cambridge, USA, and is a recipient of a Draper Laboratory Fellowship. His research interests include optical properties of materials, nanofabrication and flat optical devices.

Charles Roques-Carmes was born in Besançon, France, in 1994. He received the Diploma of Gradué d'Ingénierie (bachelor level) and the Diploma of "Ingénieur de l'Ecole polytechnique," (master level) majoring in physics, from the Ecole Polytechnique, Palaiseau France, in September 2015 and September 2016, respectively. Since September 2016, he has been working toward the Ph.D. degree in electrical engineering and computer science at MIT, Cambridge, MA.

From September 2013 to April 2014, he served as an Officer for the Gendarmerie Nationale in Meaux, french military police force. In 2015, he was a Summer Intern for attocube systems AG, Munich. In 2016, he was a Research Intern in the Capasso Group, Harvard SEAS, on dielectric metasurfaces. His research interests include dielectric metasurfaces, correction of chromatic aberrations in metasurfaces, characterization and correction of geometrical aberrations in metasurfaces, and 3-D printed optics and quantum information processing.

Ishan Mishra was born in Varanasi, India, in 1997. He is currently working toward the B.A.Sc. degree in nanotechnology engineering at the University of Waterloo, Canada.

Since May 2016, he has been a Research Assistant at Harvard University's Faculty of Engineering and Applied Sciences, where he was involved with the development of planar metalenses.

Federico Capasso is the Robert Wallace Professor of applied physics at Harvard University, which he joined in 2003 after 27 years at Bell Labs where his career advanced from Postdoctoral Fellow to Vice President for Physical Research. He and his group have made wide ranging contributions to optics, photonics, and nanotechnology, including pioneering the bandgap engineering technique, the invention of the quantum cascade laser, the first measurement of the repulsive Casimir force and more recently research on metasurfaces and their applications, including the generalized Snell's law and flat lenses. He is a member of the National Academy of Sciences, the National Academy of Engineering, the American Academy of Arts and Sciences (AAAS), and a foreign member of the Accademia dei Lincei. His awards include the IEEE Edison Medal, the American Physical Society Arthur Schawlow Prize, the King Faisal Prize, the SPIE Gold Medal, the AAAS Rumford Prize, the IEEE Sarnoff Award, the Materials Research Society Medal, the Franklin Institute Wetherill Medal, the European Physical Society Quantum Electronics Prize, the Rank Prize in Optoelectronics, the Optical Society Wood Prize, the Berthold Leibinger Future Prize, the Julius Springer Prize in applied physics, the Institute of Physics Duddell Medal, the Jan Czochralski Award for lifetime achievements in materials science, and the Gold Medal of the President of Italy for meritorious achievement in science.